

# The Mars Topside Ionosphere Response to the X8.2 Solar Flare of 10 September 2017

E.M.B. Thiemann<sup>1</sup>, L. Andersson<sup>1</sup>, R. Lillis<sup>2</sup>, P. Withers<sup>3</sup>, S. Xu<sup>2</sup>, M. Elrod<sup>4,5</sup>, S. Jain<sup>1</sup>, M.D. Pilinski<sup>1</sup>, D. Pawlowski<sup>6</sup>, P.C. Chamberlin<sup>1</sup>, F.G. Eparvier<sup>1</sup>, M. Benna<sup>4,7</sup>, C. Fowler<sup>1</sup>, S. Curry<sup>2</sup>, W.K. Peterson<sup>1</sup>

<sup>1</sup>Laboratory for Atmospheric and Space Physics, University of Colorado, Boulder, USA

<sup>2</sup>Space Sciences Laboratory, University of California, Berkeley, USA.

<sup>3</sup>Center for Space Physics, Boston University, Boston, Massachusetts, USA.

<sup>4</sup>NASA Goddard Space Flight Center, Greenbelt, Maryland, USA.

<sup>5</sup>CRESSTII University of Maryland, College Park, MD, USA

<sup>6</sup>Physics Department, Eastern Michigan University, Ypsilanti, USA.

<sup>7</sup>CRESSTII University of Maryland Baltimore County, Baltimore County, MD, USA

Corresponding author: Ed Thiemann ([thiemann@lasp.colorado.edu](mailto:thiemann@lasp.colorado.edu))

## Key Points:

- Ionizing EUV flux increased by 170% at the flare peak, causing changes in the observed (>150 km) plasma density, temperature and composition.
- Ionospheric changes are a result of an expanded neutral atmosphere, and the increased relative abundance of O at fixed pressure level.
- Photochemical escape of O increased moderately for observations made 80 minutes after the flare peak.

This article has been accepted for publication and undergone full peer review but has not been through the copyediting, typesetting, pagination and proofreading process which may lead to differences between this version and the Version of Record. Please cite this article as doi: 10.1029/2018GL077730

## Abstract

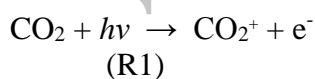
On 10 September 2017, irradiance from a Magnitude X8.2 solar flare impacted Mars while the Mars Atmosphere and Volatile Evolution (MAVEN) orbiter was characterizing the Mars upper atmosphere. This solar flare was the largest to occur during the MAVEN mission to-date, nearly tripling the ionizing irradiance impacting Mars in tens of minutes, and provides an opportunity to study the planet's response to extreme irradiance changes. This letter reports in-situ observations of the Mars topside ionosphere's response to this flare above 155 km made 1.67 hours after the flare soft x-ray peak. The observed plasma density increase is higher than expected based solely on increased ionization, and the electron temperature decreases below 225 km; both effects can be explained by an expanded neutral atmosphere, which efficiently dissipates any flare induced heating of the thermal electrons at altitudes where CO<sub>2</sub> is the dominant species. Further, the ion density and composition changes significantly at both fixed altitude and pressure-level, which can be explained by a change in the O:CO<sub>2</sub> density ratio, highlighting the importance this ratio has in determining ionospheric structure.

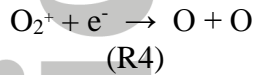
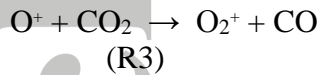
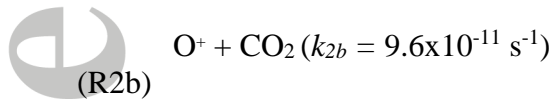
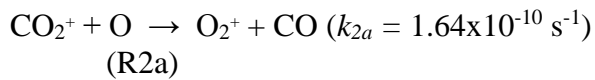
## 1 Introduction

Solar flares are the result of the rapid conversion of magnetic energy to kinetic energy in the solar corona, producing emissions from hot loops of plasma. Many of these emissions originate from atomic line transitions at extreme ultraviolet (EUV, 10-120 nm) wavelengths, and thermal bremsstrahlung at soft x-ray (SXR, 0.1-10 nm) wavelengths. Flares have spatial scales comparable to those of sunspots; and are short-lived, typically lasting tens of minutes. Flares are classified by their irradiance (incident power per area) in the 0.1-0.8 nm range as Common (C), Moderate (M) and Extreme (X), with historical occurrence rates of 1367 yr<sup>-1</sup>, 195 yr<sup>-1</sup> and 14 yr<sup>-1</sup>, respectively [Veronig *et al.*, 2002].

At Mars, flare irradiance ionizes and heats the upper atmosphere [Gurnett *et al.*, 2005; Thiemann *et al.*, 2015], similar to what occurs at Earth [Donnelly, 1967; Qian *et al.*, 2011]. Flare irradiance initially affects the ionosphere by increasing the photoionization rate, with the largest increase occurring near ~100 km, where highly energetic photoelectrons subsequently further ionize the atmosphere through impact ionization [Lollo *et al.*, 2012; Peterson *et al.*, 2016]. The ionospheric plasma density enhancement generally tracks the flare ionizing irradiance enhancement [Mendillo *et al.*, 1974]. The added energy is then transferred from the plasma to the neutral constituents through a series of collisions and chemical reactions [Fox and Dalgarno, 1979], resulting in heating and subsequent expansion of the neutral atmosphere. The time-response of the neutral atmosphere is somewhat delayed and more long-lived than that of the ionosphere, a result of the neutral atmosphere's non-negligible heat capacity [Thiemann *et al.*, 2015].

The electron density structure of the Martian ionosphere is similar to that of Earth [e.g. Witasse *et al.*, 2008]. There is a peak in electron density ( $n_e$ ) corresponding with the altitude of peak EUV irradiance absorption near ~125 km (termed the M2 layer and similar to Earth's F region), and a shoulder near ~100 km corresponding with the altitude of peak SXR absorption (termed the M1 layer and similar to Earth's E region). Although CO<sub>2</sub> is the major neutral species in the Mars atmosphere below ~220-230 km, the major ion species is O<sub>2</sub><sup>+</sup> because CO<sub>2</sub><sup>+</sup> rapidly reacts with other species according to the three following reactions [Kumar and Hunten, 1974; Fox and Dalgarno, 1979]:





where  $h\nu$  is photon energy,  $e^-$  is an electron, and reaction rates ( $k_R$ ) are given in R2a and R2b. Therefore, below ~220-230 km, where  $\text{CO}_2$  is the major species,  $\text{O}_2^+$  is the terminal ion species produced by photoionization, which may subsequently dissociatively recombine to form O. Additionally, increased irradiance at Far Ultraviolet (FUV) wavelengths will photodissociate  $\text{CO}_2$ , primarily yielding CO and O [McElroy and McConnell; 1971].

Because solar flares are transient, studying how the Mars atmosphere responds to them can lead to a better understanding of processes that maintain the chemical, thermal and charge structure of the Martian upper atmosphere. Additionally, because EUV irradiance variability has been implicated as a major controlling factor in atmospheric escape rates [Ergun *et al.*, 2016; Dubinin *et al.*, 2017; Lillis *et al.*, 2017], understanding how the Mars atmosphere responds to solar flares is important for understanding the evolution of the Mars atmosphere, particularly during its earliest epochs, when flaring activity of the young Sun is expected to have been substantially more prevalent [Lammer *et al.*, 2006].

A number of studies have investigated how the Mars upper atmosphere responds to solar flares, with much of the literature concentrating on observations from radio occultation (RO) measurements made by the Mars Global Surveyor (MGS) orbiter [Mendillo *et al.*, 2006; Mahajan *et al.*, 2010; Fallows *et al.*, 2015], which retrieved vertical  $n_e$  between ~80-200 km, showing substantial enhancements of the M1 layer of the ionosphere during flares. The response of the Mars neutral atmosphere to solar flares was investigated by Thiemann *et al.*, [2015], who used in-situ observations from the Mars Atmosphere and Volatile Evolution (MAVEN) probe to show that the Mars neutral atmosphere expands quickly as the temperature increases from solar flare heating.

There have been few past modeling studies of the Mars atmosphere response to solar flares. Lollo *et al.*, [2012] simulated MGS RO observations with some success, accurately reproducing the large  $n_e$  enhancement near 110 km, but under-predicting the enhancement between ~80-100 km. Recently, Haider *et al.*, [2016] simulated the ion production from 80 to 200 km during a solar flare, predicting a ~10-100× increases in  $n_e$  and  $\text{O}_2^+$  density at 200 km. The authors then predicted Integrated Electron Content (IEC) values, which were substantially larger than the MGS RO IEC measurements that they compared against.

This letter reports observations made by MAVEN of the response of the Mars upper atmosphere to a magnitude X8.2 flare. For context, this flare is the largest to occur while MAVEN has been at Mars, and the second largest known to have occurred during the current 11-year solar cycle [Chamberlin *et al.*, 2018]. MAVEN observes the thermal plasma environment in-situ with the Langmuir Probe and Waves (LPW) [Andersson *et al.*, 2015] and Neutral Gas and Ion Mass Spectrometer (NGIMS) [Mahaffy *et al.*, 2015] instruments, both of

which observed significant changes in the topside ionosphere as a result of this flare at MAVEN measurement altitudes (>155 km). These are the first reported observations of changes in the thermal plasma environment measured in-situ at Mars and the first-ever observations of the Martian ion response to solar flare forcing. This flare was followed by a large solar energetic particle event and interplanetary coronal mass ejection [C. Lee *et al.*, 2018]. However, these other events arrived at Mars a number of hours or days after the flare, allowing for the results reported here to be unambiguously attributed to the flare irradiance.

This letter aims to guide the reader through the 10 September 2017 flare's impact on the Mars topside ionosphere as observed by MAVEN, beginning with solar irradiance observations, followed by model results of flare induced ionization and energy deposition, and concluding with a presentation of how the structure of the ionosphere is altered as a result of the flare. In Section 2, the observations and data reduction methods are described. MAVEN measurements of the topside ionosphere response are presented in Section 3, and the results are interpreted and discussed in Section 4, which includes a simulation of how photochemical escape was impacted by the flare. Conclusions are stated in Section 5.

**2 Data and Methods** Spectral irradiance estimates at Mars at 0.1 nm resolution are derived from combined observations made by the MAVEN EUV Monitor (EUVM) [Eparvier *et al.*, 2015] and Earth-based instruments. Wavelengths between 0.05 and 36 nm, except 30.4 nm, are estimated by the Synthetic Reference spectra (SynRef) spectral irradiance model [Thiemann, 2016], which is analogous to the X-ray Photometer System (XPS; Woods *et al.* 1999; 2005) Level 4 spectral irradiance models [Woods *et al.*, 2008], but driven by EUVM measurements using updated references spectra. Note, the SynRef flare irradiance model requires a flare plasma temperature as an input, which is provided using (Earth-based) Geostationary Operational Environmental Satellites (GOES) X-Ray Sensor (XRS) [Bornmann *et al.*, 1996] measurements using the methods of Thomas *et al.*, 1985 and White *et al.*, 2005. 30.4 nm irradiances are estimated using EUVM 121.6 nm measurements, which are scaled and offset by regression coefficients, computed from a dataset of 886 30.4 nm and 121.6 nm peak-flare irradiance measurements made by the Multiple EUV Grating Spectrograph (MEGS)-A channel of the EUV Variability Experiment (EVE) [Woods *et al.*, 2010] onboard the Solar Dynamics Observatory (SDO) and the GOES-15 EUV Spectrograph (EUVS)-E channel [Vioreck *et al.*, 2007]. The Pearson correlation coefficient between the two data-sets is 0.89 with a slope of 0.178 (30.4 nm irradiance / 121.6 nm irradiance). Flare irradiance from 36.1 to 106 nm is measured directly by the EVE MEGS-B channel, which observed the flare from Earth at 0.1 nm resolution. The routine EUVM Level 3 (L3) spectra are used above 106 nm.

The EUVM L3 spectral irradiance model [Thiemann *et al.*, 2017] is not used to estimate the 10 September 2017 flare irradiance below 106 nm because the linear relationship between flare irradiance in the 0.1-1 nm band and the 0.1-7 nm band, the latter of which is used as an input to the L3 irradiance model, is atypical for this flare. The atypical relationship was identified by comparing the ratio of the 0.1-7 nm channel of the EUV SpectroPhotometer (ESP) [Didkovsky *et al.*, 2009] onboard SDO to the 0.1-0.8 nm channel of the GOES XRS with the expected ratio reported by Hock *et al.*, [2013].

The data sources for the spectral irradiance estimates described above are as follows: The EUVM SynRef model uses EUVM Level 2 (L2) Corrected Counts, Version 11, Revision 1 with GOES-15 XRS temperatures retrieved from the SolarSoft [Freeland and Handy, 1998] *goes* object. The XRS flare temperatures are scaled by 0.7 to correct for a hot temperature bias in the XRS temperature recently reported by Ryan *et al.*, [2014]. The EUVM L2 Calibrated Irradiance, Version 11, Revision 1 is used for the 30.4 nm bin irradiance model, using

regression coefficients found between the SDO EVE L2 Version 6 and the GOES-15 EUVS-E Version 4 data products. The direct MEGS-B flare irradiance measurements are from the SDO EVE L2 Version 6 data product. From 106 to 195 nm, the EUVM L3 Spectral Model, Version 11, Revision 1 is used.

Electron density and temperature ( $n_e$ ,  $T_e$ ) of the Mars ionosphere are found using in-situ measurements from MAVEN LPW. LPW makes measurements of the ionosphere every orbit near periapsis, which occurs at  $\sim 4.5$  hour intervals. On 10 September 2017, MAVEN periapsis occurred near 17:30 Local Solar Time and  $32^\circ$  N (geographic coordinates); and the solar zenith angle varied from  $65.9^\circ$  to  $68.5^\circ$  during the inbound orbit segment. The 10 September 2017 flare irradiance peaked near 16:24 and the nearest post-peak in-situ ionospheric measurements occurred near 17:40 during orbit 5718. Only measurements from the in-bound periapsis orbit segment are reported here because they were made nearer to the sub-solar point, where flare induced changes are more pronounced. The data used here are from the L2 lpw.derived:data.lp.nt collection, Version 3, Revision 4. The sampling cadence is 4 seconds, which corresponds with  $\sim 1.5$  km vertical resolution at 200 km. These data are smoothed with a 5-sample moving average (to reduce fine-scale variability and noise).

Number density for  $O_2^+$ ,  $CO_2^+$  and  $O^+$  are measured in-situ by the MAVEN NGIMS instrument. NGIMS made ion measurements of the ionosphere every other orbit near periapsis, at  $\sim 9$  hour intervals. Serendipitously, NGIMS made ion observations during the orbit 5718 periapsis. The data used here are from the L2 Version 7, Revision 1 ion abundance data product. The sampling cadence is 2 seconds, which corresponds with  $\sim 0.7$  km vertical resolution at 200 km. These data are also smoothed with a 5-sample moving average.

Ionospheric measurements are plotted versus altitude and pressure in Section 3, the latter of which must be computed independently. Here, pressure is found using MAVEN NGIMS  $CO_2$  and O measurements reported in the L2 Version 7, Revision 3 neutral abundance data product, which are measured every orbit below 500 km. Pressure at a given height is found by vertically integrating the NGIMS derived major species vertical mass column using the method described in Thiemann *et al.*, [2018].

### 3 Results

A time-series of ionizing 0-91 nm solar EUV irradiance ( $E_{91}$ ) is shown in Figure 1a during the 10 September 2017 flare. Prior to the flare,  $E_{91}$  is near  $1.2$  mW/m<sup>2</sup>. Near 16:00 UT,  $E_{91}$  begins to rapidly increase, reaching a value of  $\sim 3.2$  mW/m<sup>2</sup> within  $\sim 10$  minutes, where it remains for  $\sim 24$  minutes, prior to beginning to decay.  $E_{91}$  then returns to half of its maximum value after  $\sim 36$  minutes, and after 1 hour, returns to a quarter of its maximum value.

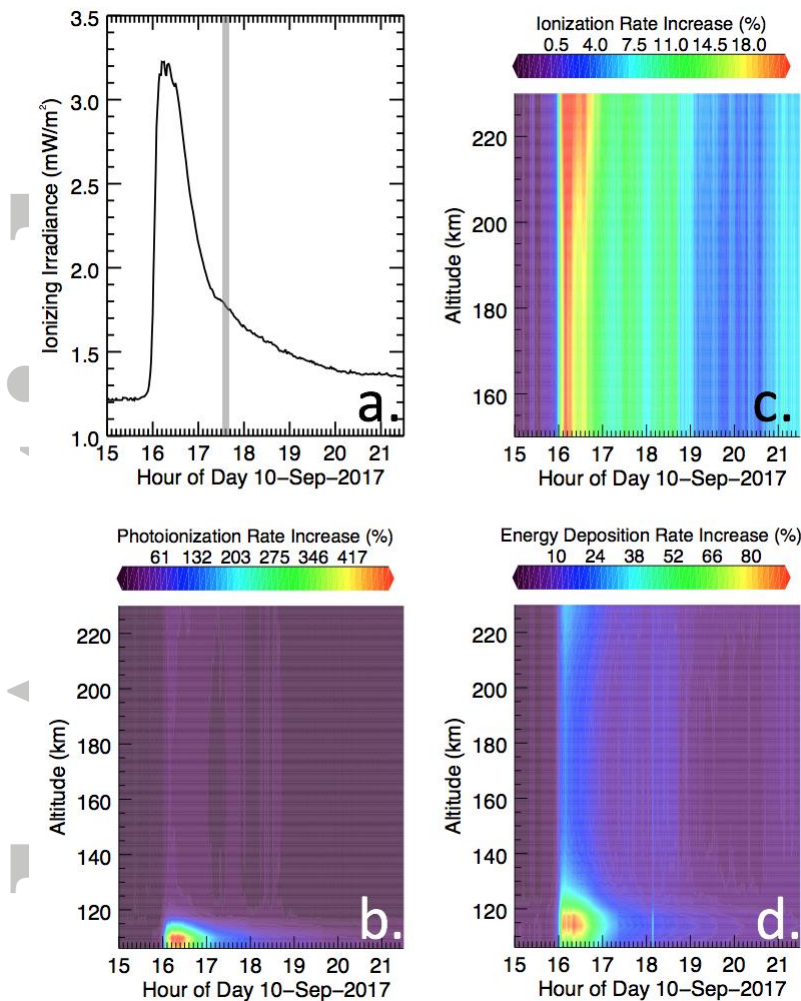


**Figure 1.** Solar flare EUV irradiance forcing by the 10 September 2017 flare. **a)** The 0-91 nm solar EUV irradiance during the flare. The vertical bar indicates the timing of the inbound periapsis orbit segment. **b)** The modeled photoionization rate increase from 105 to 230 km. **c)** The modeled ionization rate increase above 155 km, corresponding with MAVEN in-situ measurement altitudes. **d)** The modeled energy deposition rate increase from 105 to 230 km.

The altitude at which this irradiance is absorbed depends on the irradiance spectrum and atmospheric composition. These variables are taken into account in Figures 1b-1d, which show the enhancement of the ionization rate (energy deposition rate) versus altitude in Figures 1b-1c (1d). For each time and altitude interval, these simulations first compute the local irradiance by attenuating the topside irradiance according to extinction by the column of absorbers along the line-of-sight. Then, the photoionization (energy deposition) rate per unit volume is computed by using irradiance in units of photons/area-time (power/area) and photoionization (photo-absorption) cross-sections of the constituent gases. Static CO<sub>2</sub> and O atmospheric profiles are used in these calculations, and are comprised of the pre-flare MAVEN periapsis observations from orbit 5717 above 155 km, and contemporaneous neutral density predictions by the Mars Global Ionosphere Thermosphere Model (MGITM) [Bougher *et al.*, 2015] below 155 km. Atmospheric cross-sections were downloaded from the PHoto Ionization/Dissociation Rates database at <http://phidrates.space.swri.edu> [Huebner *et al.*, 1992]. Figure 1b shows that the photoionization rate enhancement peaks near 110 km, and is 500% larger than the pre-flare photoionization rate. Note, the total ionization rate increase is larger than that in Figure 1c because many of the primary photoelectrons are highly energetic

and further ionize the atmosphere via impact ionization [Xu *et al.*, 2018]. Figure 1c shows the ionization rate increase of the topside ionosphere, and the maximum enhancement is briefly near ~20% at the flare peak and then sustained between ~10% and 15% for the decaying phase of the flare. The ionization increase of the topside ionosphere increases with altitude because O becomes the major species at higher altitudes, and since O cross-sections are biased to shorter wavelengths relative to CO<sub>2</sub> cross-sections, O is more sensitive to (short wavelength dominated) flare enhancements than CO<sub>2</sub>. Figure 1d shows the enhancement of the energy deposition rate per unit volume, which peaks near ~100% at 115 km. The energy deposition enhancement extends to high altitudes, with values near 30%, and becomes more prominent in the O dominated region of the upper atmosphere. The reason for both the higher peak absorption altitude and smaller relative magnitude of the energy deposition enhancement compared to the ionization enhancement is because CO<sub>2</sub> absorbs (non-ionizing) photons well into the FUV. However, the FUV is not as significantly enhanced during flares [Chamberlin *et al.*, 2008], and deposits energy at lower altitudes. Thus, the relative energy deposition enhancement at shorter flare wavelengths results in larger relative enhancements at higher altitudes.

Values of  $n_e$  ( $T_e$ ) are plotted in Figures 2a and 2b (2c and 2d) versus altitude and pressure, respectively. The measurements for orbit 5718 are shown with thick red curves, and those for orbit 5719 (~4.5 hours later) are shown with salmon-colored curves. Consecutive orbits immediately preceding the flare are shown with gray curves, and the average of these is shown with a thick black curve. From Figures 1a and 1c, it is apparent that, at fixed altitude, the solar flare causes an increase in  $n_e$  at all altitudes and a decrease in  $T_e$  below ~225 km. At 200 km,  $n_e$  increases by ~100% and  $T_e$  decreases by 25% from the respective daily averages. These flare-associated effects dissipate by orbit 5719. However, when looking at these same data versus pressure, as shown in Figures 2b and 2d, the flare induced effects for orbit 5718 are within the variability of the surrounding orbits, although there is a steep temperature increase at pressures below  $5 \times 10^{-8}$  Pa. Note, the rapid increase of  $T_e$  and decrease of  $n_e$  in orbit 5719 above 225 km are likely a result of disturbed solar wind [C. Lee *et al.*, 2018].

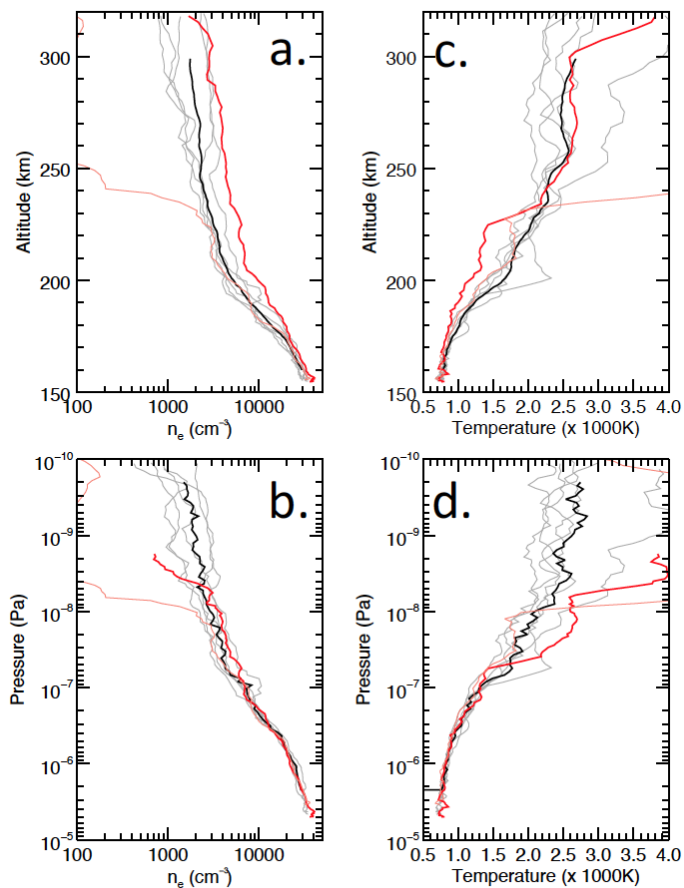


**Figure 2.** LPW observations of thermal electron density (**a** and **b**) and temperature (**c** and **d**) for orbits surrounding the 10 September 2017 flare. Density and temperature are plotted versus altitude (**a** and **c**) and pressure (**b** and **d**). Orbits preceding the flare are plotted with grey curves and their average is plotted with thick black curves, the flare orbit is plotted with thick red curves, and the orbit immediately following the flare is plotted with salmon-colored curves.

NGIMS density measurements versus altitude (pressure) of  $O_2^+$ ,  $CO_2^+$  and  $O^+$  are shown in Figure 3a (3b).  $n_e$  is shown in Figure 3a for comparison. The color code is the same as in Figure 2, except measurements were not made for orbit 5719 due to ion measurements being made on alternating orbits. Orbits 5714, 5716 and 5720 are shown with gray curves. From Figure 3a, it is apparent that densities for all three species increase by up to 100% above their average values for the measurements made immediately after the flare peak, with  $O_2^+$ ,  $CO_2^+$  increasing at all altitudes and  $O^+$  increasing above 220 km. Also, the  $O^+$  density reversal occurs at lower altitudes for orbit 5718, near 305 km, while it occurs near 325 km for the average profile. Note, the discrepancy between  $O_2^+$  and  $n_e$  is within the mutual uncertainties of NGIMS and LPW and thus, charge neutrality is assumed to hold. From Figure 3b, there is a substantial change in the  $O^+$  density profile versus pressure during Orbit 5718: The peak density increases by  $\sim 150\%$  and the density reversal occurs at a  $\sim 50\times$  higher pressure level, resulting in a substantial narrowing of the  $O^+$  profile in both pressure and altitude coordinates. At pressures above that of the  $O^+$  density reversal ( $>10^{-8}$  Pa), the  $O_2^+$  density for orbit 5718 follows the average profile, but at the location of the  $O^+$  density reversal, the  $O_2^+$  density profile diverges, resulting in a more rapid decrease with pressure for orbit 5718. The change in absolute density of the  $CO_2^+$  profile during orbit 5718 is within the variability seen in other orbits, but the slope (in pressure coordinates) of the  $CO_2^+$  is markedly different for orbit 5718,

showing a more rapid decrease with pressure of  $\text{CO}_2^+$ . Figure 3c shows the corresponding O: $\text{CO}_2$  density versus pressure coordinates. This ratio becomes increasingly larger than average with decreasing pressure for orbit 5718 below  $10^{-7}$  Pa.

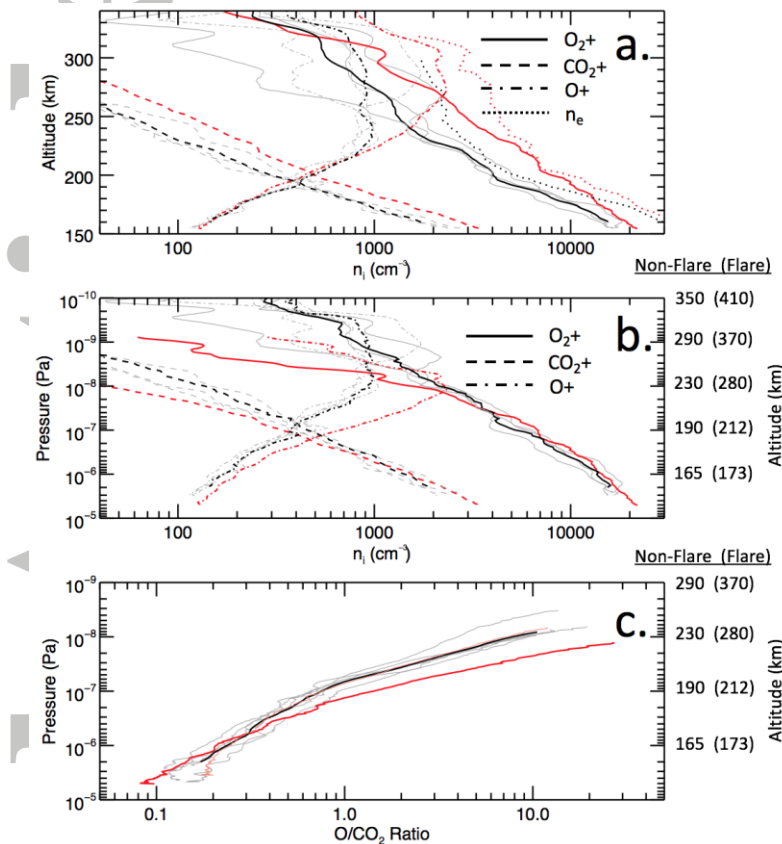


**Figure 3.** NGIMS ion observations for orbits surrounding the 10 September 2017 flare plotted versus altitude (a) and pressure (b). Line-styles indicate plasma species according to the legend. Thick red curves correspond with the orbit immediately following the flare peak. Gray curves correspond with orbits surrounding the flare, with the thick black curve corresponding with their average. c) The corresponding O/ $\text{CO}_2$  neutral density ratio.

## 4 Discussion

Elrod *et al.*, [2018] showed that the neutral atmosphere expands significantly for orbit 5718 as a result of flare heating, which explains why some of the observed changes versus altitude in  $n_e$ ,  $T_e$  and  $\text{O}_2^+$  largely disappear when viewed versus pressure. For example,  $T_e$  is markedly lower below 225 km for orbit 5718 in Figure 2c but, at fixed pressure, nearly matches its average value (above  $5 \times 10^{-8}$  Pa) in Figure 2d. Taken together, these data indicate that the temperature change at fixed altitude is consistent with an inflated thermosphere shifting both the neutral and plasma density profiles upwards. Further, the steep increase in  $T_e$  near 225 km corresponds with altitudes where O becomes the dominant major neutral species. As such, this feature is likely the result of thermal electron cooling by O being substantially (~98%) less efficient than that by  $\text{CO}_2$  [Schunk and Nagy, 2009]. Additionally, at 180 km, Figure 1c predicts an 11% increase in  $n_e$  during orbit 5718 due to increased photoionization, whereas the measured increase was ~45%; the difference is attributed to an inflated thermosphere, with  $\text{CO}_2$  densities increasing by ~50% at 180 km.

Figure 3c shows the O: $\text{CO}_2$  density ratio increases with decreasing pressure for orbit 5718, likely a result of enhanced photodissociation, photoionization and subsequent electron

impact ionization from the flare. Note that although flare spectral energy enhancements are typically largest at ionizing wavelengths, the number of photons increases more at FUV wavelengths, resulting in both ionizing and dissociative processes being important contributors to O production during flares.

Neglecting transport (a questionable approximation above ~180 km where transport becomes increasingly important with altitude) and assuming photochemical equilibrium, we can approximate from (R1)-(R2b),

$$Pn_{CO_2} = (k_{2a} + k_{2b})n_{CO_2^+}n_O \quad (1)$$

where P is the photo-production rate of  $CO_2^+$ . Similarly, from (R2b)-(R3), we have

$$n_{CO_2^+}n_Ok_{2b} = k_3n_{CO_2}n_{O^+}. \quad (2)$$

It follows that  $n_{O^+} \propto n_O/n_{CO_2}$ , while  $n_{CO_2^+} \propto n_{CO_2}/n_O$ . Therefore, enhancing the O:CO<sub>2</sub> density ratio will enhance production of  $O^+$  while suppressing production of  $CO_2^+$ . Further, reducing the fraction of CO<sub>2</sub> at fixed pressure should reduce production of  $O_2^+$  by photoionization of CO<sub>2</sub>.

These observations are in general agreement with the simulations of Lollo *et al.*, [2012], who showed a ~5% ionization enhancement above 155 km, when considering that they did not account for the expanding neutral atmosphere. However, the simulated flare induced ion density enhancements by Haider *et al.*, [2016], who predicted ~10× and 100× enhancements in  $O_2^+$  and  $CO_2^+$  density at 200 km, are inconsistent with these observations. These observations indicate that the neutral atmosphere plays an important role in determining the structure of the topside ionosphere after solar flares, and simulations should take this into account, as is done in recent simulations by Xu *et al.* [2018] and Fang *et al.* [2018].

Photochemical escape of O is believed to be one of the major pathways for atmospheric loss at Mars in the current epoch [Lammer *et al.*, 2009]. It occurs through dissociative recombination of  $O_2^+$  (Reaction (R4)), which can produce a "hot" O atom with sufficient velocity to escape Mars's atmosphere [Nagy and Cravens, 1988]. The likelihood for a newly formed O atom to escape at a particular altitude depends on the abundance of  $O_2^+$ , the neutral column density along the (upward) trajectory and  $T_e$ . Lillis *et al.*, [2017] developed a model for photochemical escape of O, using MAVEN measurements as inputs. This model is used here to simulate O escape for all orbits in September 2017 in order to characterize the relative change in the escape rate due to the flare. These results are shown in Figure 4a and 4b, which show the O escape flux and the escaping O production rate, respectively, for September with the flare orbit indicated by red color. This simulation shows that the escape flux increases to above the 99th percentile and, hence, is unlikely to simply be the result of stochastic variability. Further, 4b shows a substantial change in the escaping O production rate altitude profile. Taken together, Figures 4a and 4b indicate the flare shifted the escaping O production significantly upward, yielding a moderate enhancement in (vertically integrated) loss. Although photochemical escape over the dayside hemisphere has minimal dependence on solar zenith angle (SZA) [Lillis *et al.*, 2017], care should be taken extrapolating these simulation results to global flare-induced escape rate because solar flare effects are expected to be strongly dependent on SZA [Qian *et al.* 2011; Y. Lee *et al.*, 2018].

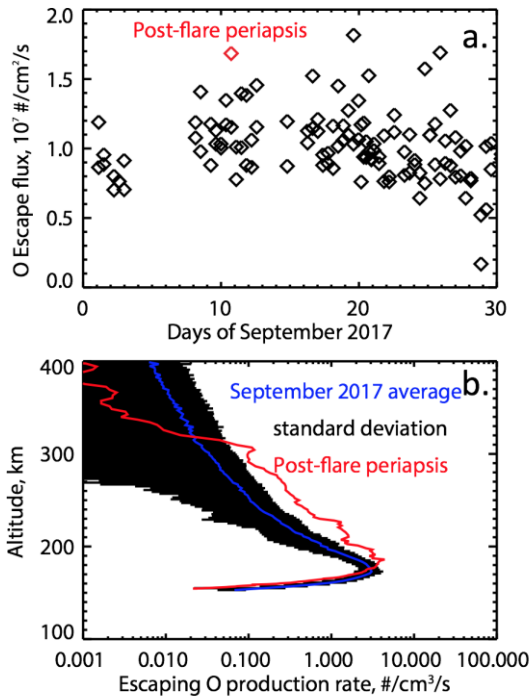


**Figure 4.** Simulations of photochemical escape of O for September 2017. **a)** Total escape flux with the orbit 5718 indicated in red. **b)** Escaping O production rate versus altitude with orbit 5718 shown in red.

## 5 Summary and Conclusions

Changes in the topside ionosphere due to the 10 September 2017 flare are influenced by interactions between the charged and neutral constituents of the upper atmosphere: Initially, the solar flare ionizes the atmosphere, predominantly around 110 km, and increased FUV irradiance increases photodissociation of  $\text{CO}_2$ . This results in photoelectron heating of the neutral atmosphere and increased production of O, increasing the relative O abundance. The hot expanded neutral atmosphere increases plasma density at fixed altitude via enhanced photoionization rates, while decreasing  $T_e$ . The increased O/ $\text{CO}_2$  ratio with pressure changes the ion composition in the topside ionosphere, increasing the concentration of  $\text{O}^+$  above  $\sim 10^{-8}$  Pa, while decreasing both  $\text{O}^+$  and  $\text{O}_2^+$  at pressures below  $\sim 10^{-8}$  Pa. Below 225 km, efficient cooling of the thermal electrons by collisions with  $\text{CO}_2$  rapidly dissipates any flare induced heating, but  $T_e$  enhancements persist above 225 km, where O is the dominant species.

The following can be concluded from this study on the effect large solar flares have on the Mars ionosphere:

1. Large solar flares can have a significant impact on the density and composition of the Martian topside ionosphere even though the majority of ionization occurs at lower altitudes.
2. Plasma density enhancements at fixed altitude are sustained for over an hour after the flare peak by an inflated neutral atmosphere.
3. The enhanced relative O abundance restructures the composition and density of the topside ionosphere.

4. Large solar flares result in moderate increases in photochemical escape.

### **Acknowledgments, Samples, and Data**

MAVEN data used in this study are available through the NASA Planetary Data System at <https://pds.nasa.gov>. Photo-absorption and -ionization cross-sections were downloaded from the Southwest Research Institute's <http://phidrates.space.swri.edu> webpage.

EMBT would like to thank Dr. C. Lee of the University of California, Berkeley for helpful discussions regarding the September 2017 solar storm.

This work was supported by the NASA MAVEN project through the Mars Exploration Program. D. Pawlowski thanks NASA for their support under grant NNX16AJ54G.

The irradiance spectra for this flare are available through the public MAVEN Science Data Center website at <https://lasp.colorado.edu/maven/sdc/public/pages/datasets/euv.html>.

### **References**

Andersson, L., Ergun, R. E., Delory, G. T., Eriksson, A., Westfall, J., Reed, H., ... & Meyers, D. (2015). The Langmuir probe and waves (LPW) instrument for MAVEN. *Space Science Reviews*, 195(1-4), 173-198.

Bornmann, P. L., Speich, D., Hirman, J., Matheson, L., Grubb, R., Garcia, H. A., & Viereck, R. (1996, October). GOES X-ray sensor and its use in predicting solar-terrestrial disturbances. In *GOES-8 and Beyond* (Vol. 2812, pp. 291-299). International Society for Optics and Photonics.

Bougher, S. W., Pawlowski, D., Bell, J. M., Nelli, S., McDunn, T., Murphy, J. R., ... & Ridley, A. (2015). Mars Global Ionosphere-Thermosphere Model: Solar cycle, seasonal, and diurnal variations of the Mars upper atmosphere. *Journal of Geophysical Research: Planets*, 120(2), 311-342.

Chamberlin, P. C., Woods, T. N., & Eparvier, F. G. (2008). Flare irradiance spectral model (FISM): Flare component algorithms and results. *Space Weather*, 6(5).

Chamberlin, P.C., Woods, T.N., Didkovsky, L., Eparvier, F.G., Jones, A.R., Mason, J.P., Machol, J., Snow, M., Thiemann, E.M.B., Viereck, R., & Woodraska, D. (2018). Solar Ultraviolet Irradiance Observations of the Solar Flares During the Intense September 2017 Storm Period. *Space Weather*, in prep.

Didkovsky, L., Judge, D., Wieman, S., Woods, T., & Jones, A. (2009). EUV spectrophotometer (ESP) in extreme ultraviolet variability experiment (EVE): algorithms and calibrations. In *The Solar Dynamics Observatory* (pp. 179-205). Springer, New York, NY.

Donnelly, R. F. (1967). The solar flare radiations responsible for sudden frequency deviations. *Journal of Geophysical Research*, 72(21), 5247-5256.

Dubin, E., Fraenz, M., Pätzold, M., McFadden, J., Mahaffy, P. R., Eparvier, F., ... & Vaisberg, O. (2017). Effects of solar irradiance on the topside ionosphere and oxygen ion escape at Mars. MAVEN observations. *Journal of Geophysical Research: Space Physics*.

Elrod, M.K, Curry, S.M, Thiemann, E.M.B, Jain, S.K. (2018) September 2017 Solar Flare Event: Rapid Heating of the Martian Neutral Exosphere from the X-class flare as observed by MAVEN. *Geophysical Research Letters*, This Issue, submission number, 2018GL077729

Eparvier, F. G., Chamberlin, P. C., Woods, T. N., & Thiemann, E. M. B. (2015). The solar extreme ultraviolet monitor for MAVEN. *Space Science Reviews*, 195(1-4), 293-301.

Ergun, R. E., Andersson, L. A., Fowler, C. M., Woodson, A. K., Weber, T. D., Delory, G. T., ... & Stewart, A. I. F. (2016). Enhanced O<sup>2+</sup> loss at Mars due to an ambipolar electric field from electron heating. *Journal of Geophysical Research: Space Physics*, 121(5), 4668-4678.

Fang, X., D. Pawlowski, Y. Ma, E. Thiemann, C. Dong, S. Bougher, F. Eparvier, D. Brain, Y. Dong, P. Chamberlin, M. Benna, M. Elrod, P. Mahaffy, W. Wang, and B. Jakosky (2018). Global simulation of Mars upper atmospheric effects of the 10 September 2017 solar flare. *Geophysical Research Letters*, This Issue, submitted

Fallows, K., Withers, P., & Gonzalez, G. (2015). Response of the Mars ionosphere to solar flares: Analysis of MGS radio occultation data. *Journal of Geophysical Research: Space Physics*, 120(11), 9805-9825.

Fox, J. L., & Dalgarno, A. (1979). Ionization, luminosity, and heating of the upper atmosphere of Mars. *Journal of Geophysical Research: Space Physics*, 84(A12), 7315-7333.

Freeland, S. L., & Handy, B. N. (1998). Data analysis with the SolarSoft system. *Solar Physics*, 182(2), 497-500.

Gurnett, D. A., Kirchner, D. L., Huff, R. L., Morgan, D. D., Persoon, A. M., Averkamp, T. F., ... & Picardi, G. (2005). Radar soundings of the ionosphere of Mars. *Science*, 310(5756), 1929-1913.

Haider, S. A., Batista, I. S., Abdu, M. A., Santos, A. M., Shah, S. Y., & Thirupathaiiah, P. (2016). Flare X-ray photochemistry of the E region ionosphere of Mars. *Journal of Geophysical Research: Space Physics*, 121(7), 6870-6888.

Hock, R. A., Woodraska, D., & Woods, T. N. (2013). Using SDO EVE data as a proxy for GOES XRS B 1–8 angstrom. *Space Weather*, 11(5), 262-271.

Huebner, W. F., Keady, J. J., & Lyon, S. P. (1992). Solar photo rates for planetary atmospheres and atmospheric pollutants. In *Solar photo rates for planetary atmospheres and atmospheric pollutants* (pp. 1-289). Springer Netherlands.

Kumar, S., & Hunten, D. M. (1974). Venus: An ionospheric model with an exospheric temperature of 350 K. *Journal of Geophysical Research*, 79(16), 2529-2532.

Lammer, H., Kulikov, Y. N., & Lichtenegger, H. I. (2006). Thermospheric X-ray and EUV heating by the young Sun on early Venus and Mars. *Space Science Reviews*, 122(1-4), 189-196.

Lammer, H., Kasting, J. F., Chassefière, E., Johnson, R. E., Kulikov, Y. N., & Tian, F. (2008). Atmospheric escape and evolution of terrestrial planets and satellites. *Space Science Reviews*, 139(1-4), 399-436.

Lee, C., et al. (2018), Observations and Impacts of the 10 September 2017 Solar Events at Mars: An Overview. *Geophysical Research Letters*, This Issue, submitted

Lee, Y., Dong, C., Pawlowski, D., Tenishev, V., Mahaffy, P., Benna, M., Combi, M., Bougher, S., Eparvier, F. & Thiemann, E. Effects of a Solar Flare on the Martian Hot O Corona and Photochemical Escape. *Geophysical Research Letters*, This Issue, submitted

Lollo, A., Withers, P., Fallows, K., Girazian, Z., Matta, M., & Chamberlin, P. C. (2012). Numerical simulations of the ionosphere of Mars during a solar flare. *Journal of Geophysical Research: Space Physics*, 117(A5).

Mahaffy, P. R., Benna, M., King, T., Harpold, D. N., Arvey, R., Barciniak, M., ... & Johnson, C. S. (2015). The neutral gas and ion mass spectrometer on the Mars atmosphere and volatile evolution mission. *Space Science Reviews*, 195(1-4), 49-73.

Mahajan, K. K., Lodhi, N. K., & Upadhyaya, A. K. (2010). Observations of X-ray and EUV fluxes during X-class solar flares and response of topside ionosphere. *Journal of Geophysical Research: Space Physics*, 115(A12).

McElroy, M. B., & McConnell, J. C. (1971). Dissociation of CO<sub>2</sub> in the Martian atmosphere. *Journal of the Atmospheric Sciences*, 28(6), 879-884.

Mendillo, M., Klobuchar, J. A., Fritz, R. B., Da Rosa, A. V., Kersley, L., Yeh, K. C., ... & Schödel, J. P. (1974). Behavior of the ionospheric F region during the great solar flare of August 7, 1972. *Journal of Geophysical Research*, 79(4), 665-672.

Mendillo, M., Withers, P., Hinson, D., Rishbeth, H., & Reinisch, B. (2006). Effects of solar flares on the ionosphere of Mars. *Science*, 311(5764), 1135-1138.

Nagy, A. F., & Cravens, T. E. (1988). Hot oxygen atoms in the upper atmospheres of Venus and Mars. *Geophysical research letters*, 15(5), 433-435.

Peterson, W. K., Thiemann, E. M., Eparvier, F. G., Andersson, L., Fowler, C. M., Larson, D., ... & Xu, S. (2016). Photoelectrons and solar ionizing radiation at Mars: Predictions versus MAVEN observations. *Journal of Geophysical Research: Space Physics*, 121(9), 8859-8870.

Qian, L., Burns, A. G., Chamberlin, P. C., & Solomon, S. C. (2011). Variability of thermosphere and ionosphere responses to solar flares. *Journal of Geophysical Research: Space Physics*, 116(A10).

Ryan, D. F., O'Flannagain, A. M., Aschwanden, M. J., & Gallagher, P. T. (2014). The compatibility of flare temperatures observed with AIA, GOES, and RHESSI. *Solar Physics*, 289(7), 2547-2563.

Schunk, R., & Nagy, A. (2009). *Ionospheres: physics, plasma physics, and chemistry*. Cambridge university press.

Thiemann, E. M. B., Eparvier, F. G., Andersson, L. A., Fowler, C. M., Peterson, W. K., Mahaffy, P. R., ... & Deighan, J. I. (2015). Neutral density response to solar flares at Mars. *Geophysical Research Letters*, 42(21), 8986-8992.

Thiemann, E. M. (2016). Multi-spectral sensor driven solar EUV irradiance models with improved spectro-temporal resolution for space weather applications at Earth and Mars. *Doctoral dissertation, University of Colorado at Boulder*, ProQuest Dissertations & Theses, Order No. 10150855.

Thiemann, E., Chamberlin, P. C., Eparvier, F. G., Templeman, B., Woods, T. N., Bougher, S. W., & Jakosky, B. M. (2017). The MAVEN EUVM model of solar spectral irradiance variability at Mars: Algorithms and results. *Journal of Geophysical Research: Space Physics*, 122(3), 2748-2767.

Thiemann, E. M. B., Eparvier, F. G., Bougher, S. W., Dominique, M., Andersson, L., Girazian, Z., ... & Jakosky, B. M. (2018). Mars Thermospheric Variability Revealed by MAVEN EUVM Solar Occultations: Structure at Aphelion and Perihelion, and Response to EUV Forcing. *arXiv preprint arXiv:1802.02189*.

Thomas, R. J., Starr, R., & Crannell, C. J. (1985). Expressions to determine temperatures and emission measures for solar X-ray events from GOES measurements. *Solar physics*, 95(2), 323-329.

Viereck, R., Hanser, F., Wise, J., Guha, S., Jones, A., McMullin, D., ... & Evans, S. (2007, September). Solar extreme ultraviolet irradiance observations from GOES: design characteristics and initial performance. In *Solar Physics and Space Weather Instrumentation II* (Vol. 6689, p. 66890K). International Society for Optics and Photonics.

Veronig, A., Temmer, M., Hanslmeier, A., Otruba, W., & Messerotti, M. (2002). Temporal aspects and frequency distributions of solar soft X-ray flares. *Astronomy & Astrophysics*, 382(3), 1070-1080.

White, S. M., Thomas, R. J., & Schwartz, R. A. (2005). Updated expressions for determining temperatures and emission measures from GOES soft X-ray measurements. *Solar Physics*, 227(2), 231-248.

Witasse, O., Cravens, T., Mendillo, M., Moses, J., Kliore, A., Nagy, A. F., & Breus, T. (2008). Solar system ionospheres. In *Comparative Aeronomy* (pp. 235-265). Springer, New York, NY.

Woods, T. N., Rodgers, E. M., Bailey, S. M., Eparvier, F. G., & Ucker, G. J. (1999, October). TIMED solar EUV experiment: preflight calibration results for the XUV photometer system. In *Optical Spectroscopic Techniques and Instrumentation for Atmospheric and Space Research III* (Vol. 3756, pp. 255-265). International Society for Optics and Photonics.

Woods, T. N., Rottman, G., & Vest, R. (2005). XUV Photometer System (XPS): overview and calibrations. In *The Solar Radiation and Climate Experiment (SORCE)* (pp. 345-374). Springer, New York, NY.

Woods, T. N., Chamberlin, P. C., Peterson, W. K., Meier, R. R., Richards, P. G., Strickland, D. J., ... & Mannucci, A. J. (2008). XUV Photometer System (XPS): Improved solar irradiance algorithm using CHIANTI spectral models. *Solar Physics*, 250(2), 235-267.

Woods, T. N., Eparvier, F. G., Hock, R., Jones, A. R., Woodraska, D., Judge, D., ... & McMullin, D. (2010). Extreme Ultraviolet Variability Experiment (EVE) on the Solar Dynamics Observatory (SDO): Overview of science objectives, instrument design, data products, and model developments. In *The Solar Dynamics Observatory* (pp. 115-143). Springer, New York, NY.

Xu, S., Thiemann, E., Mitchell, D., Eparvier, F., Pawlowski, D., Benna, M., Andersson, L., Liemohn, M., Bougher, S., & Mazelle, C. (2018) Observations and modeling of low-altitude ionospheric response to the 2017 September solar flare at Mars. *Geophysical Research Letters*, This Issue, Submission number 2018GL077709

Accepted Article